



# The clustering morphology of freely rising deformable bubbles

Yoshiyuki Tagawa<sup>1,3,†</sup>, Ivo Roghair<sup>2</sup>, Vivek N. Prakash<sup>1</sup>, Martin van Sint Annaland<sup>2</sup>, Hans Kuipers<sup>2</sup>, Chao Sun<sup>1,†</sup> and Detlef Lohse<sup>1,†</sup>

<sup>1</sup>Physics of Fluids Group, Faculty of Science and Technology, J. M. Burgers Centre for Fluid Dynamics, University of Twente, PO Box 217, 7500 AE Enschede, The Netherlands

<sup>2</sup>Multiphase Reactors Group, Department of Chemical Engineering and Chemistry, J. M. Burgers Centre for Fluid Dynamics, Eindhoven University of Technology, PO Box 513, 5600 MB Eindhoven, The Netherlands

<sup>3</sup>Department of Mechanical Systems Engineering, Tokyo University of Agriculture and Technology, 1848588, Koganei-city, Tokyo, Japan

(Received 4 December 2012; revised 8 February 2013; accepted 17 February 2013; first published online 18 March 2013)

---

We investigate the clustering morphology of a swarm of freely rising deformable bubbles. A three-dimensional Voronoï analysis enables us to distinguish quantitatively between two typical preferential clustering configurations: a regular lattice arrangement and irregular clustering. The bubble data are obtained from direct numerical simulations using the front-tracking method. It is found that the bubble deformation, represented by the aspect ratio  $\chi$ , plays a significant role in determining which type of clustering is realized: nearly spherical bubbles form a regular lattice arrangement, while more deformed bubbles show irregular clustering. Remarkably, this criterion for the clustering morphology holds for different diameters of the bubbles, surface tensions and viscosities of the liquid in the studied parameter regime. The mechanism of this clustering behaviour is most likely connected to the amount of vorticity generated at the bubble surfaces.

**Key words:** bubble dynamics, drops and bubbles, multiphase and particle-laden flows

---

## 1. Introduction

Particles dispersed in a flow can distribute inhomogeneously, showing clustering or preferential concentration behaviour. This is attributed to the interaction between the two phases, and the inertia of the particles (Calzavarini *et al.* 2008; Toschi & Bodenschatz 2009). A swarm of bubbles rising in a quiescent liquid is a subset of the general case of particles dispersed in a complex flow. This topic of bubbly flow

† Email addresses for correspondence: [tagawayo@cc.tuat.ac.jp](mailto:tagawayo@cc.tuat.ac.jp), [c.sun@utwente.nl](mailto:c.sun@utwente.nl), [d.lohse@utwente.nl](mailto:d.lohse@utwente.nl)

has applications in bubble columns, which are important in the chemical industry, in chemical processes such as oxidation and chlorination in water treatment, and in the steel industry (Deen *et al.* 2000). Freely rising bubbles in an originally still liquid are known to induce liquid velocity fluctuations that result in the so-called ‘pseudo-turbulence’. Bubble clustering in pseudo-turbulence has attracted much attention because of its importance in applications and the lack of understanding of the fundamental physics (Zenit, Koch & Sangani 2001; Martínez Mercado *et al.* 2010; Riboux, Risso & Legendre 2010; Roghair *et al.* 2011). Bunner & Tryggvason (2002, 2003) have conducted numerical simulations and found that deformability of the bubbles plays an important role in the clustering phenomenon: bubbles with small deformability (spherical bubbles) show a horizontal alignment, while deformed bubbles display clustering in the vertical direction. Meanwhile, experiments have found both horizontal and vertical clustering, depending on parameters such as bubble deformation, size and other flow properties (Cartellier & Rivière 2001; Zenit *et al.* 2001; Martínez Mercado *et al.* 2010).

In the present work, the bubble data are obtained from direct numerical simulations (DNSs) of a swarm of rising bubbles. The bubble clustering in the same dataset was previously studied using the angular pair correlation (Roghair, Annaland & Kuipers 2012*b*). Here, we revisit the issue of bubble clustering, using a Voronoi analysis technique, which has been proven to be a powerful tool for quantifying the clustering behaviour of bubbles and particles in fluid flow (see e.g. Monchaux, Bourgoin & Cartellier 2010; Fiabane *et al.* 2012; Tagawa *et al.* 2012). We extend the Voronoi analysis to study the geometric morphology of the clusters formed by freely rising deformable bubbles.

## 2. Voronoi analysis for clustering morphology of bubbles

In the method of Voronoi tessellations, each Voronoi cell is defined at a particle location based on its neighbours (Okabe *et al.* 2000). Every point inside a Voronoi cell is the nearest to the particle location compared to the neighbours; the exceptions being border lines, vertices and facets, which have the same distance between two or more particles. In a given three-dimensional distribution of particles, if the volume of the Voronoi cells is smaller compared to the cells in neighbouring regions, then the particles belong to a clustering region. It has been found that a  $\Gamma$  distribution can well describe the probability density functions (p.d.f.s) of the Voronoi volumes of randomly distributed particles in three-dimensions (Ferenc & Néda 2007), namely

$$f(x) = \frac{3125}{24} x^4 \exp(-5x), \quad (2.1)$$

where  $x = \mathcal{V}/\overline{\mathcal{V}}$  is the Voronoi volume  $\mathcal{V}$  normalized by the mean volume  $\overline{\mathcal{V}}$ . Such a random distribution of particles, and their corresponding Voronoi cells, are shown in the upper panel of figure 1(*b*). In the lower panel of figure 1(*b*), the corresponding  $\Gamma$  distribution fitted p.d.f. is shown. Particles that are not randomly distributed will have a p.d.f. that deviates from this  $\Gamma$  distribution.

Figure 1 shows examples of different particle arrangements. In figure 1(*a*), the particles prefer to aggregate in a small central region, accompanied by void regions. We refer to this situation as ‘irregular clustering’. In this case, the probabilities of small and large Voronoi volumes are higher than the  $\Gamma$  distribution. In figure 1(*c*) particles keep the same distance between each other, having the same size Voronoi cells. Therefore, the size distribution becomes narrower compared to the case

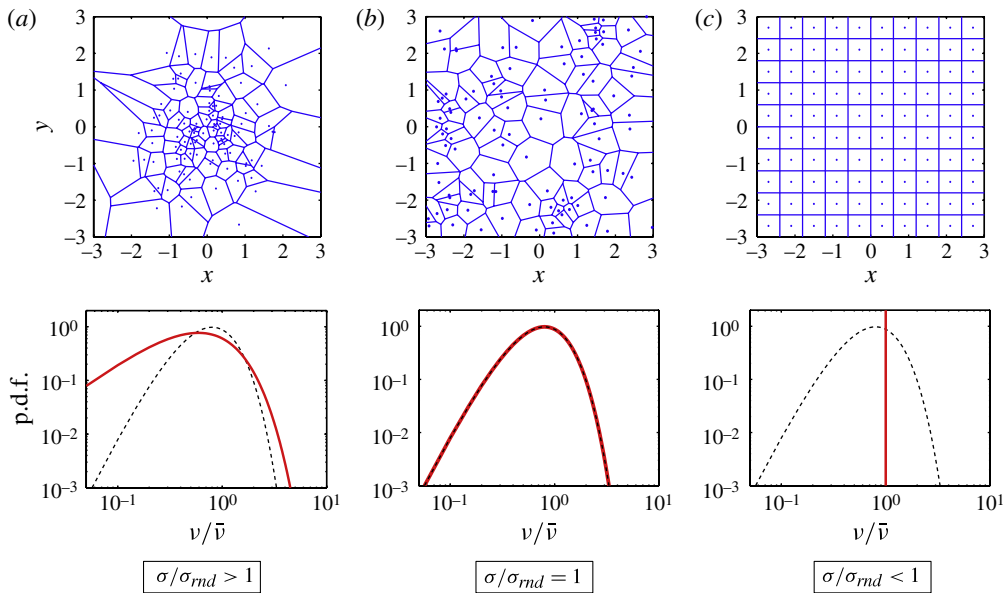


FIGURE 1. Examples of the different types by which a fixed number (in this case 100) of particles can be spatially distributed: (a) irregular clustering (b) random distribution, and (c) regular lattice arrangement. The upper panels show the Voronoi tessellations based on the particle positions in two dimensions, for ease of illustration. The lower panels show the corresponding p.d.f.s of the Voronoi volumes (the three-dimensional case). In each case, the p.d.f. corresponding to the upper panel (thick red line) is compared with the p.d.f. of the randomly distributed particles (dashed black line). The value of the clustering indicator (i.e. the standard deviation of the p.d.f. normalized by that of randomly distributed particles,  $\sigma/\sigma_{rnd}$ ) is also shown below the p.d.f.

of randomly distributed particles. We refer to this situation as a ‘regular lattice arrangement’. Tagawa *et al.* (2012) found that these distributions can be well fitted by a  $\Gamma$  distribution with a single fitting parameter  $\sigma$ , which is the standard deviation of Voronoi volumes. Furthermore, this parameter  $\sigma$  can be used to quantify the particle clustering. In this work, we use  $\sigma$  to investigate the morphology of the bubble clustering. Here  $\sigma$  is normalized by the standard deviation of randomly distributed particles  $\sigma_{rnd}$ . The indicator is (see figure 1)  $\sigma/\sigma_{rnd} > 1$  for irregular clustering,  $\sigma/\sigma_{rnd} = 1$  for a random distribution, and  $\sigma/\sigma_{rnd} < 1$  for a regular lattice arrangement.

In the application of the Voronoi analysis on the present numerical data, there are two specific issues that are addressed below. First, the Voronoi cells of particles located near the edges of the domain are not well defined, i.e. the Voronoi cells either do not close or close at points outside of the domain. These Voronoi cells located near the domain edges are usually discarded from the Voronoi analysis (as in Tagawa *et al.* 2012). However, in the present data, the number of bubbles in the domain is small. In this case, we cannot afford to ignore the edge cells, as doing so will result in poor statistics. We take advantage of the periodic boundary condition of the numerics to overcome this problem. The periodic boundary condition enables us to form a box ( $3 \times 3 \times 3$  larger, and including all particles) surrounding the original box. We then apply the three-dimensional Voronoi tessellation on the particle positions in this larger

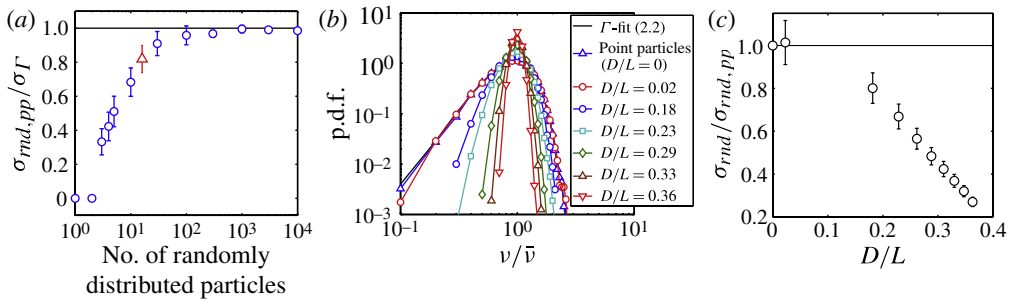


FIGURE 2. (a) The standard deviation of Voronoi volumes as a function of the number of randomly distributed point-like particles in a periodic box. The standard deviations are normalized by the standard deviation  $\sigma_\Gamma = 0.4472$  for an infinite number of particles ( $>10^6$ ) in a box, as shown by Ferenc & Néda (2007). In the present datasets, we consider 16 bubbles in a periodic box, and the corresponding data point is indicated by the red triangle. (b) The p.d.f.s of Voronoi volumes for randomly distributed spheres at different sphere–domain length ratios  $D/L$ . The  $\Gamma$  fit for 16 spheres expressed by (2.2) with  $\sigma_{md,pp}$  (thin black line) and the p.d.f. for randomly distributed point-like particles agree well. The shape of the p.d.f.s becomes narrower with increasing  $D/L$  due to the finite-size effect. (c) The standard deviations of Voronoi volumes  $\sigma_{rnd}$  normalized by that for the point-particle case  $\sigma_{rnd,pp}$  as a function of  $D/L$ . The value  $\sigma_{rnd}/\sigma_{rnd,pp}$  decreases with increasing  $D/L$ .

box. We can now ignore the cell edges on this larger box, as we have a sufficient number of particles for good statistics. Also, if one considers the central box, although some Voronoi cells protrude into the neighbouring boxes, the total volume is still conserved owing to the periodic boundary conditions. This is an added advantage of this method.

Secondly, the number of particles available for the Voronoi analysis is a key parameter that can significantly affect the results (see figure 6 in Tagawa *et al.* (2012)). We check the dependence of the number of particles on the standard deviation of Voronoi volumes in figure 2(a) for randomly distributed point-like particles. We vary the number of particles inside each of the boxes that are replicated to form the larger box as mentioned above. The Voronoi tessellations are applied, and the standard deviation of Voronoi volumes for each case of the varying number of particles is shown in figure 2(a). Also, the standard deviation of Voronoi volumes is normalized by that of randomly distributed particles with numbers  $>10^6$  (Ferenc & Néda 2007). Each error bar has been calculated by repeating this procedure more than  $10^4$  times. We see in figure 2(a) that, when the particle number is less than 100, the value of the standard deviation changes quite significantly. We note the peculiarity that, when a box includes just one or two particle(s), the Voronoi volumes are the same or half of the volume of the domain, respectively, and hence the standard deviation is zero. For a larger number of particles, the standard deviation grows with increasing number of particles, shows an asymptotic behaviour, and saturates to the value of unity when the particle numbers approach  $\sim 1000$ . In previous work (Tagawa *et al.* 2012) we have used a value of  $\sigma/\sigma_\Gamma = 1$  for the Voronoi analysis, as we had 1000 particles in our simulations. In the present work, the number of bubbles used in the numerical simulations is 16. In this case, figure 2(a) gives the corresponding value of the standard deviation as  $\sigma_{rnd,pp}/\sigma_\Gamma = 0.82$ . We account for this change by

Case no.	Diameter $D$ (mm)	Void fraction $\alpha$ (%)	Sphere–domain ratio $D/L$	Kinematic viscosity $\nu$ ( $\times 10^{-6}$ m <sup>2</sup> s <sup>-1</sup> )	Surface tension $\gamma$ (mN m <sup>-1</sup> )
1–3	1.0	10, 25, 40	0.23, 0.31, 0.36	1	73
4	1.0	10	0.23	5	73
5	1.0	10	0.23	1	7.3
6–11	2.0	5–40	0.18–0.36	1	73
12–18	2.5	5–40	0.18–0.36	1	73
19–26	3.0	5–40	0.18–0.36	1	73
27–33	3.5	5–40	0.18–0.36	1	73

TABLE 1. Summary of the simulation parameters.

using  $\sigma_{md,pp} = 0.82\sigma_r$  in the equation that describes the Voronoï volume p.d.f. fit using the single parameter  $\sigma$  (Tagawa *et al.* 2012):

$$f(x) = \frac{1}{\sigma^{(2/\sigma^2)} \Gamma\left(\frac{1}{\sigma^2}\right)} x^{(1/\sigma^2)-1} \exp^{-(x/\sigma^2)}. \quad (2.2)$$

This equation indeed results in a nice fit, as shown in figure 2(b), where we plot the Voronoï volume p.d.f. for 16 randomly distributed particles (blue upward-pointing triangles) and the curve from (2.2) (thin black line).

All the above discussions were devoted to point-like particles, but in this study we consider bubbles with a finite size ( $D = 1\text{--}3.5$  mm). Table 1 lists the different parameters used in the numerics. Thus, we need first to understand the effect of finite particle size on the Voronoï volume distributions. For this, we artificially generate random positions in three dimensions (see § 3) for 16 perfect spheres of diameter  $D$  and change the domain size  $L$  to vary the sphere–domain length ratio  $D/L$ . This sphere–domain length ratio  $D/L$  is related to the void fraction  $\alpha$  by the expression  $D/L = (3\alpha/8\pi)^{1/3}$ . For clarity of presentation, we have chosen to describe the clustering results using  $D/L$  instead of  $\alpha$ . In figure 2(b) we show the Voronoï volume p.d.f.s for the 16 randomly distributed spheres at different  $D/L$ . The p.d.f. of the Voronoï volume for the randomly distributed point particles and for spheres at the small value of  $D/L = 0.02$  show quite a similar behaviour, i.e. the finite-size effect is then negligible. The finite-size effects become more significant with increasing  $D/L$ , and this is seen in the shape of the p.d.f. The p.d.f.s become narrower with increasing  $D/L$ , implying that the bubbles are distributed more evenly throughout the domain. At a large value of  $D/L$ , each of the spheres occupies a relatively larger volume in the box, which reduces the available free space (for other spheres), leading to a more constrained distribution and narrower p.d.f. shape.

The standard deviations of the Voronoï volume p.d.f.s as a function of  $D/L$  are shown in figure 2(c). The values  $\sigma_{md}$  are normalized by the standard deviation obtained from the  $\Gamma$  distribution fit for randomly distributed point particles,  $\sigma_{md,pp}$ . The indicator  $\sigma_{md}/\sigma_{md,pp}$  decreases monotonically with  $D/L$ , starting at 1 (at  $D/L = 0$ ) and reducing to  $\sim 1/5$  for  $D/L = 0.36$ , clearly indicating the effect of finite size. The normalization of the clustering indicator  $\mathcal{C} = \sigma(D/L)/\sigma_{md}(D/L)$  for each case used in the discussion below is carried out at the same bubble–domain length ratio  $D/L$ , in order to fully focus on dynamical effects. For the case of deformable bubbles to be discussed below, there will be variations in the bubble eccentricity, which is difficult

to take into account while defining a standard case for normalization of the clustering indicator. Hence, we choose the reference case of artificially generated spheres to present our results below.

### 3. Numerical method

Three-dimensional DNSs have been performed to simulate bubbles rising in a swarm, using periodic boundary conditions in all directions to mimic an ‘infinite’ swarm without wall effects, similarly to what has been done by Bunner & Tryggvason (2002). The simulations have been carried out using a model that incorporates the front-tracking (FT) method (Unverdi & Tryggvason 1992), which tracks the interfaces of the bubbles explicitly using Lagrangian control points distributed homogeneously over the interface. Compared to interface reconstruction techniques, such as volume-of-fluid or level-set methods, the advantage of the FT method is that the bubbles are able to approach each other closely (within the size of one grid cell) and can even collide, while preventing (artificial) merging of the interfaces. Therefore, the size of the bubbles remains constant throughout the simulation. Especially for bubble swarm simulations with high void fractions as studied in this work, this is an important aspect. In addition, the interface is sharp, allowing the surface tension force to act at the exact position of the interface.

In our model (see Dijkhuizen *et al.* (2010) and Roghair *et al.* (2011a) for details), the fluid flow is solved by the discretized incompressible Navier–Stokes equations on an Eulerian background mesh consisting of cubic computational cells:

$$\rho \frac{\partial \mathbf{u}}{\partial t} + \rho \nabla \cdot (\mathbf{u}\mathbf{u}) = -\nabla p + \rho \mathbf{g} + \nabla \cdot \mu [\nabla \mathbf{u} + (\nabla \mathbf{u})^T] + \mathbf{F}_\gamma, \quad \nabla \cdot \mathbf{u} = 0, \quad (3.1)$$

where  $\mathbf{u}$  is the fluid velocity and  $\mathbf{F}_\gamma$  represents a singular source term accounting for the surface tension force at the interface (see below). The flow field of both phases is resolved using a one-fluid formulation where the physical properties are determined from the local phase fraction. The local density  $\rho$  is obtained by the weighted arithmetic mean and the dynamic viscosity  $\mu$  is obtained via the weighted harmonic mean of the kinematic viscosities. The interface between the gas and the liquid is tracked using Lagrangian control points, distributed over the interface. The control points are connected such that they form a mesh of triangular cells. The surface tension force is acquired by obtaining the pull forces for each marker  $m$  and its neighbouring cells  $i$ :  $\mathbf{F}_{\gamma, i \rightarrow m} = \gamma (\mathbf{t}_{mi} \times \mathbf{n}_{mi})$ . The shared tangent  $\mathbf{t}_{mi}$  is known from the control point locations, and the shared normal vector  $\mathbf{n}_{mi}$  is obtained by averaging the normals of marker  $m$  and neighbouring marker  $i$ . Subsequently, the surface tension force is mapped to the Eulerian background grid using mass weighing (Deen, van Sint Annaland & Kuipers 2004) at the position of the interface. After accounting for the surface tension force on all interface cells, the total pressure jump  $\Delta p$  of the bubble is obtained. The pressure jump is distributed over the bubble interface and mapped back to the Eulerian mesh. For interfaces with a constant curvature (i.e. spheres), the pressure jump and surface tension cancel each other out exactly on each marker, but if the curvature varies over the interface (which is the case for deformed bubbles), a small net force will be transmitted.

At each time step, after solving the fluid flow equations, the Lagrangian control points are advected with the interpolated flow velocity. Spatial interpolation of the flow field to the control point positions is performed by a piecewise cubic spline, and temporal integration is performed by Runge–Kutta time stepping. Since the control

points may move away from or towards each other, the interface mesh is remeshed afterwards, in order to keep the control points equally distributed on the interface (while keeping the volume enclosed by the dispersed elements constant). The edges of the triangular interface markers are kept within 0.2–0.5 times an Eulerian grid size. The total runtime for numerical simulations is about  $t = 2$  s, and the Voronoï volume time series reveals that the clustering is initially transient and settles to a quasi-steady state after  $t = 1$  s. Hence, we only consider data after  $t = 1$  s from the starting time. The clustering results are averaged over different snapshots at intervals of  $t = 0.05$  s.

Each bubble was tracked individually, using the locations of the control points on the interface to acquire the bubble position (centre of mass) and bubble shape (aspect ratio), which were stored for further analysis. The aspect ratio is calculated from the ratio between the major and the minor axes  $\chi$  along the Cartesian axes:  $\chi = \sqrt{d_x d_y} / d_z$ . Note that this procedure neglects diagonal shape deformations, so that strongly deformed bubbles oriented diagonally may be attributed an aspect ratio of  $\chi \approx 1$  (nearly spherical). In this work we consider bubbles with limited deformability and under mild flow conditions so that these effects can safely be neglected.

Simulations were performed using 16 bubbles in a periodic domain. For ellipsoidal bubbles, Bunner & Tryggvason (2002) have indicated that 12 bubbles is the minimum number of bubbles that are required to simulate bubbles rising in a swarm, based on their terminal rise velocity. The present simulations with periodic boundary conditions might not be totally comparable to real systems, as length scales larger than the size of the periodic box might not be captured accurately. The void fraction  $\alpha = V_{\text{bubbles}} / V_{\text{domain}}$  was varied from dilute ( $\alpha = 0.05$ ) up to dense void fractions of  $\alpha = 0.4$  by changing the domain size. In all simulations, the spatial resolution was determined by the bubble diameter  $1.0 \times 10^{-3} \leq d_b \leq 3.5 \times 10^{-3}$  such that the length of a cubic grid cell  $\Delta x = d_b / 20$ . The physical properties represent typical air bubbles in water conditions, i.e. a density ratio of  $\rho_{\text{liquid}} / \rho_{\text{gas}} \approx 1000$ , dynamic viscosity ratio  $\mu_{\text{liquid}} / \mu_{\text{gas}} \approx 50$  and a surface tension coefficient  $\gamma = 0.073 \text{ N m}^{-1}$ . The simulation parameters are summarized in table 1. Figure 3 provides information on the variation of (a) the aspect ratio  $\chi$  and (b) the Reynolds number  $Re$  as a function of  $D/L$ . Here, the Reynolds number is defined as  $Re = UD/\nu$ , where  $U$  is the relative velocity between the bubbles and surrounding liquid. The error bars in figure 3(a) indicate the time-averaged standard deviation of the aspect ratio for all the bubbles. We observe that the variation of  $\chi$ , indicated by the error bars, decreases with increasing  $D/L$  due to spatial restriction. The majority of the cases considered here ( $D \geq 2$  mm) correspond to Reynolds numbers  $Re > 200$ , as shown in figure 3(b). However, the Reynolds numbers are lower ( $\sim 100$ ) for the bubble sizes of  $D = 1$  mm and for special cases of high viscosity,  $Re = 12$ .

In order to avoid initialization effects from influencing our simulation results, the bubble positions were initially set to a non-ordered fashion in the domain. Especially at higher void fractions it is not efficient to subsequently place a bubble randomly in the domain without allowing overlap. Therefore, a Monte Carlo simulation procedure has been used to generate the initial positions of the bubbles, which works for all void fractions (Frenkel & Smit 2002; Beetstra 2005). First, the bubbles are placed as spheres in a structured configuration in the domain in a simple cubic configuration. Depending on the void fraction, the bubbles might overlap with each other. We now define the potential energy of the system as  $E = [|\mathbf{x}_i - \mathbf{x}_j| / (R_i + R_j)]^n$ , with a variable  $n$  characterizing how steep the potential is. The position of a bubble  $i$  is given by  $\mathbf{x}_i$  and its radius by  $R_i$ . Each bubble is now moved by a small amount in a random direction and the potential energy is determined. A move is accepted

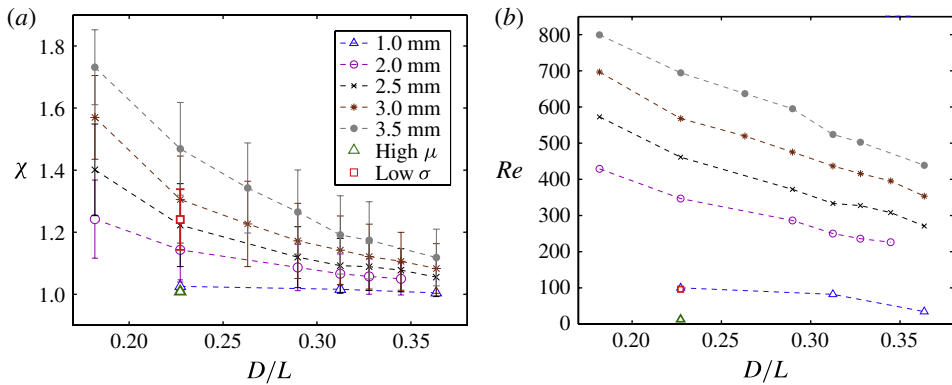


FIGURE 3. (a) The aspect ratio  $\chi$  versus bubble–domain length ratio  $D/L$ . (b) Reynolds number  $Re$  versus  $D/L$ .

whenever the potential energy remains the same or becomes less, whereas a move that increases the potential energy is accepted only if it is smaller than a critical number  $c = \exp[k(E_{old} - E_{new})]$ , where  $k$  was set to 50. In a single iteration, each bubble is allowed 200 attempts of displacement. Then, the power  $n$  is gradually increased from an initial value of 6 up to a final value of 100, and a new iteration starts. The potential energy of the system as a whole decreases during this process, and when the final state has been reached and the bubbles show no overlap at all, the positions of the bubbles are accepted for use as starting positions in the front-tracking model. Additionally, in the initial transient of the front-tracking simulations, the bubbles accelerate, deform and move through the domain, which also changes their relative positions. This start-up stage is discarded from further analysis. For the random positions of the point particles as shown in figure 2(c), the same procedure was used, except that we chose the number of allowed displacements for each particle per iteration to be  $10^4$ .

#### 4. Results and Discussions

We recall that the values of the clustering indicator  $\mathcal{C} = \sigma/\sigma_{rnd}$  are:  $\mathcal{C} > 1$  for an irregular cluster,  $\mathcal{C} = 1$  for a random distribution, and  $\mathcal{C} < 1$  for a regular lattice arrangement (figure 1). Figure 4 shows the typical bubble clustering snapshots of the side view and top view. Figure 4(a) displays a snapshot of the case of bubble diameter  $D = 1.0$  mm at  $D/L = 0.23$ . We observe horizontal clustering in one layer in the side view. The top view reveals a regular lattice arrangement, which corresponds to  $\mathcal{C} < 1$ . In figure 4(b),  $D = 1.0$  mm at  $D/L = 0.36$ , and the bubbles show horizontal clustering in a double layer, owing to larger  $D/L$  (i.e. larger void fraction  $\alpha$ ), and the value of  $\mathcal{C}$  is correspondingly less than 1. It must be noted that the shapes of the bubbles for  $D = 1.0$  mm at (a)  $D/L = 0.23$  and (b)  $D/L = 0.36$  are almost spherical. In figure 4(c), we show the case of  $D = 1.0$  mm at  $D/L = 0.23$  with lower surface tension, where the bubbles are evenly distributed throughout the domain and the horizontal one-layer clustering no longer prevails. In figure 4(d), in the case of  $D = 3.5$  mm at  $D/L = 0.36$ , the bubbles are more evenly distributed. The corresponding  $\mathcal{C}$  values for both cases are larger than 1, i.e. indicating irregular clustering. One must note that the bubbles



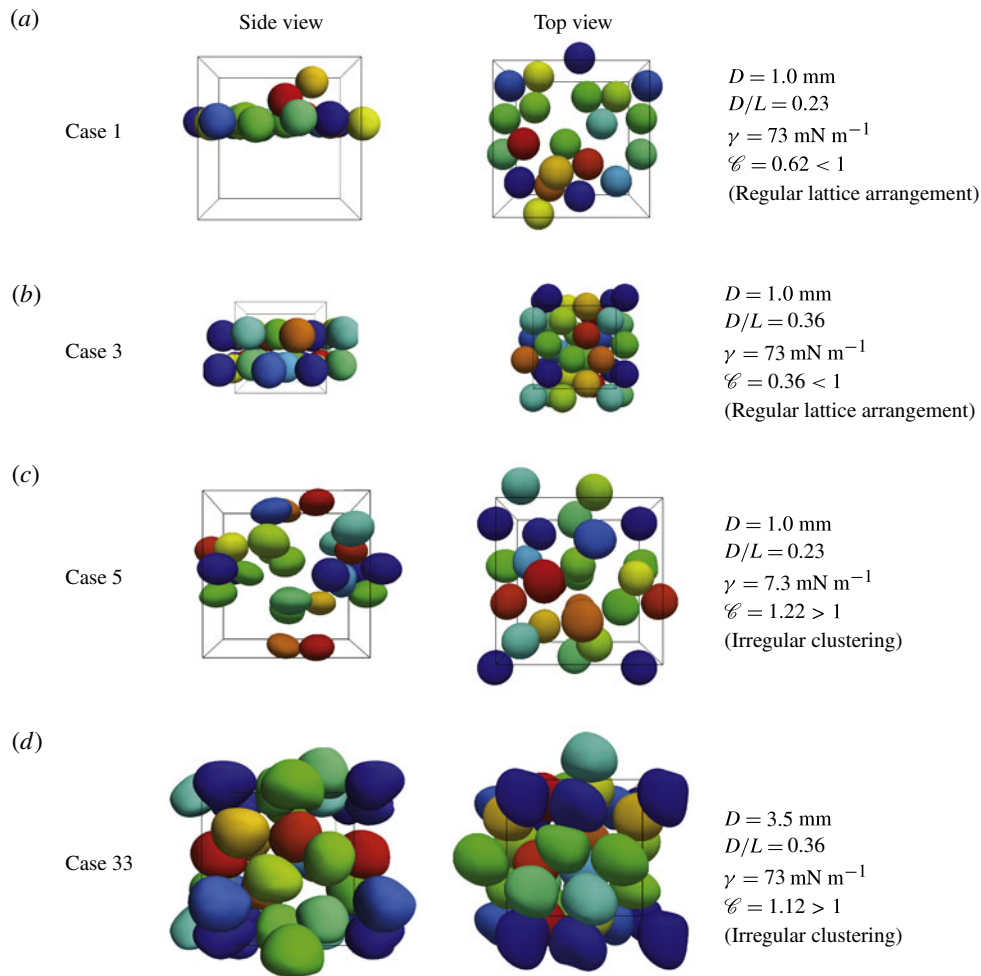


FIGURE 4. Snapshots of bubbles showing typical clustering morphologies from the side and top. The periodic box is indicated by the thin black lines. The bubbles are coloured to aid in distinguishing between individual bubbles.

with  $D = 1.0 \text{ mm}$  at  $D/L = 0.23$  with lower surface tension (panel (c)) and those with  $D = 3.5 \text{ mm}$  at  $D/L = 0.36$  have a deformed shape (panel (d)).

For a quantitative discussion, in figure 5(a) we show (as a colour contour plot) the values of the clustering indicator  $\mathcal{C}$  at different bubble–domain length ratios  $D/L$  and bubble sizes  $D$ . The data points in the parameter space (table 1) are indicated using open blue circles. The formation of regular lattice arrangements ( $\mathcal{C} < 1$ ) was only encountered in the cases of 1.0 mm diameter bubbles at  $D/L = 0.23$  and 0.36 (figure 5a). All other cases show irregular clustering ( $\mathcal{C} > 1$ ), but to a different extent.

It is well known that a rising spherical bubble with a free-slip boundary condition generates little vorticity, whereas a rising deformed bubble has a wide region of wake structure behind it (Magnaudet & Mougin 2007). The amount of vorticity generated

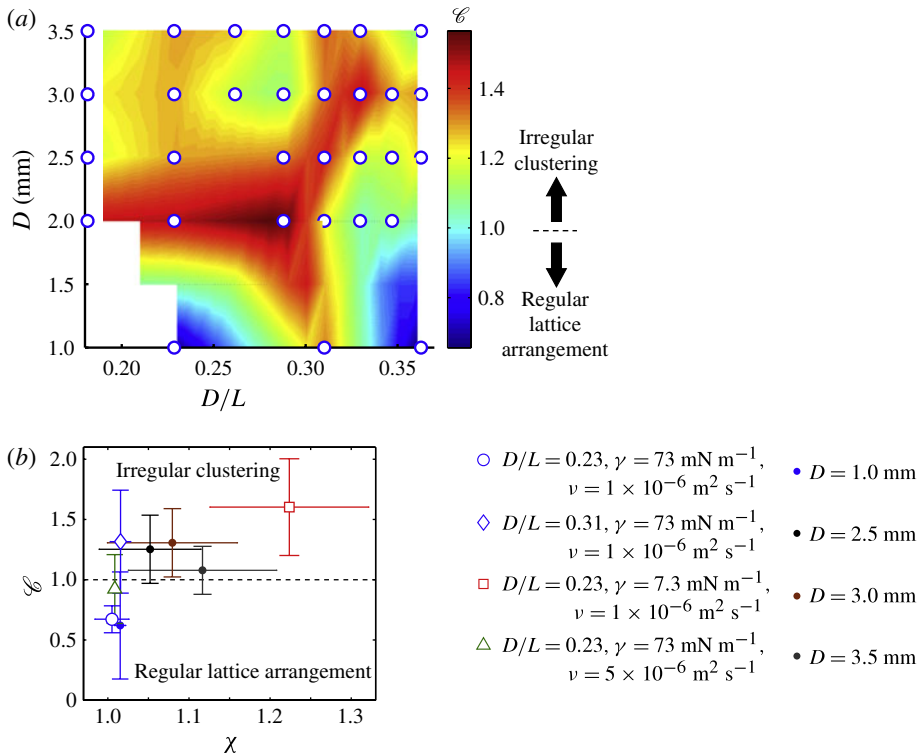


FIGURE 5. (a) Bubble clustering results: a contour plot of the clustering indicator  $\mathcal{C}$  as a function of the bubble–domain length ratio  $D/L$  for all bubble sizes  $D$  (mm). The colour bar indicates the magnitude of  $\mathcal{C}$ . All the simulation cases in table 1 are shown here except cases 4 and 5. (b) The clustering indicator  $\mathcal{C}$  as a function of the aspect ratio  $\chi$  for: fixed bubble size (open symbols),  $D = 1.0$  mm (cases 1, 2, 4, 5 in table 1); and fixed bubble–domain length ratio (solid symbols),  $D/L = 0.36$  (cases 3, 18, 26, 33 in table 1). The clustering indicator  $\mathcal{C}$  increases with increasing aspect ratio, indicating that the shape of the bubbles plays a crucial role in determining the clustering morphology. Spherical bubbles with an aspect ratio  $\chi = 1.015 \pm 0.015$  have  $\mathcal{C} < 1$ , indicating the regular lattice arrangement. All deformed bubbles with  $\chi = 1.015 \pm 0.015$  have  $\mathcal{C} > 1$ , implying irregular clustering.

from the bubbles determines the clustering morphology. The flow around spherical bubbles can be expected to be close to potential flow, containing little vorticity, and these bubbles form a regular lattice arrangement (in the horizontal plane). Deformable bubbles with larger wake regions show a greater tendency to aggregate in the vertical direction. Hence, in the discussion of the results, we focus on the bubble shape (or deformability) characterized by the bubble aspect ratio  $\chi$ . Below, we fix the size and bubble–domain length ratio, and discuss the clustering at different  $\chi$ .

Figure 5(b) shows the values of the clustering indicator  $\mathcal{C}$  as a function of the bubble aspect ratio  $\chi$ . First, we keep the bubble size constant ( $D = 1.0$  mm shown with open symbols) and discuss results for different bubble–domain length ratios, surface tensions and viscosities. The value of  $\mathcal{C}$  increases with an increase in the aspect ratio, indicating that the bubble shape is crucial for the clustering structure. We now fix the bubble–domain length ratio ( $D/L = 0.36$ ) and study the

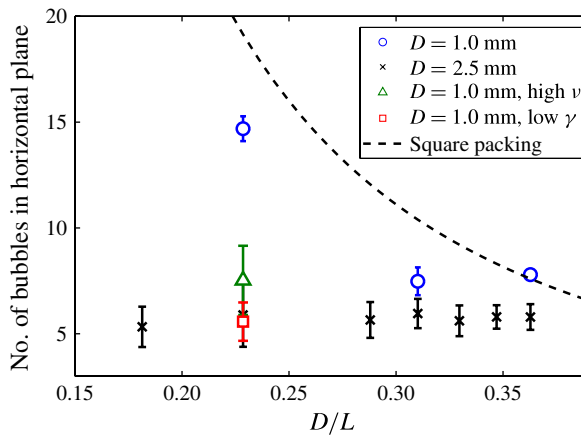


FIGURE 6. The maximum number of bubbles in a horizontal plane. The dotted line shows the values for square packing. The 1 mm bubbles (cases 1–5 in table 1) show an increasing trend with decreasing  $D/L$ , indicating that they form horizontal clusters. The 2.5 mm bubbles (cases 12–18 in table 1) show almost constant values of 6, implying that there is no horizontal clustering. The result in the case of liquid with high viscosity (case 4 in table 1, green triangle) and that for low surface tension (case 5 in table 1, red square) are also shown.

clustering behaviour for different bubble sizes shown with solid symbols in figure 5(b). Although the fixed parameter is different in this case, we still see the same trend of increasing  $\mathcal{C}$  with increasing aspect ratio  $\chi$ . Overall, we find that the shape of the bubbles is crucial for the structure of the clustering. Considering the error bars in figure 5(b), we find that the clustering transition occurs at a critical value of eccentricity,  $\chi_c = 1.015 \pm 0.015$ . Spherical bubbles with  $\chi \lesssim \chi_c$  have  $\mathcal{C} < 1$ , indicating the regular lattice arrangement. All the deformed bubbles with  $\chi \gtrsim \chi_c$  have  $\mathcal{C} > 1$ , indicating the irregular clustering morphology. In homogeneous bubbly flows at moderate particle Reynolds numbers, monodisperse spherical bubbles have been found to organize themselves into microstructures (e.g. Cartellier & Rivière 2001; Yin & Koch 2008; Cartellier, Andreotti & Sechet 2009). The physical reason is that interactions between bubbles are responsible for a slight excess of horizontal pairs, which is in agreement with present simulations at a high viscosity (case 4, see table 1).

We also quantify the intensity of horizontal clustering by counting the maximum number of bubbles at a horizontal plane, for the cases of  $D = 1$  and 2.5 mm bubbles. The bubbles are sliced at the horizontal plane and divided by the area of a circle based on the bubble radius. Figure 6 shows the maximum number of bubbles in a horizontal plane versus the bubble–domain length ratio. The line obtained from the theory of square packing is also shown for the sake of comparison. On the one hand, the 1 mm bubbles show a trend similar to the theoretical line, indicating that they organize themselves to form horizontal clusters. On the other, the 2.5 mm bubbles show almost constant values around 6, indicating the absence of horizontal clustering. The result of the lower surface tension case (case 5 in table 1) is rather close to the 2.5 mm case (case 13 in table 1) due to deformation. These results for the horizontal clustering are consistent with those obtained from the Voronoi analysis.

## 5. Conclusion

In this work, we have applied the three-dimensional Voronoï analysis on DNS data of freely rising deformable bubbles in order to investigate the clustering morphology. The numerics used a front-tracking method that allows the simulation of fully deformable interfaces of the bubbles at different diameters, bubble–domain length ratios, surface tensions and liquid viscosities. The present Voronoï analysis takes into account the effects of the number of bubbles and the finite size. It then provides a clustering indicator  $\mathcal{C} = \sigma/\sigma_{md}$ , where  $\sigma$  is the standard deviation of Voronoï volumes of the bubbles and  $\sigma_{md}$  is the standard deviation of Voronoï volumes of randomly distributed particles with finite size. We quantitatively identify two different clustering morphologies:  $\mathcal{C} > 1$  for irregular clustering and  $\mathcal{C} < 1$  for a regular lattice arrangement. Our results indicate that the bubble deformability, represented by its aspect ratio  $\chi$ , plays the most crucial role in determining the clustering morphology. A regular lattice arrangement is observed in the case of nearly spherical bubbles with  $\chi \lesssim 1.015 \pm 0.015$ . When the bubbles are deformable, for  $\chi \gtrsim 1.015 \pm 0.015$ , an irregular clustering behaviour is observed. This clustering behaviour is believed to be related to the amount of vorticity generated by the bubbles. The irregular clustering for deformed bubbles is due to the low-pressure regions in their wakes, which attract other bubbles. Spherical bubbles tend to form a regular lattice arrangement due to reduced vorticity generation.

## Acknowledgements

We thank L. van Wijngaarden for fruitful discussions. We acknowledge support from the EU COST Action MP0806 on ‘Particles in Turbulence’. We acknowledge support from the Foundation for Fundamental Research on Matter (FOM) through the FOM-IPP Industrial Partnership Program: Fundamentals of Heterogeneous Bubbly Flows.

## References

- BEETSTRA, R. 2005 Drag force in random arrays of mono- and bidisperse spheres. PhD thesis, University of Twente.
- BUNNER, B. & TRYGGVASON, G. 2002 Dynamics of homogeneous bubbly flows. Part 2. Velocity fluctuations. *J. Fluid Mech.* **466**, 17–52.
- BUNNER, B. & TRYGGVASON, G. 2003 Effect of bubble deformation on the properties of bubbly flows. *J. Fluid Mech.* **495**, 77–118.
- CALZAVARINI, E., KERSCHER, M., LOHSE, D. & TOSCHI, F. 2008 Dimensionality and morphology of particle and bubble clusters in turbulent flow. *J. Fluid Mech.* **607**, 13–24.
- CARTELLIER, A., ANDREOTTI, M. & SECHET, P. 2009 Induced agitation in homogeneous bubbly flows at moderate particle Reynolds number. *Phys. Rev. E* **80**, 065301.
- CARTELLIER, A. & RIVIÈRE, N. 2001 Bubble-induced agitation and microstructure in uniform bubbly flows at small to moderate particle Reynolds numbers. *Phys. Fluids* **13**, 2165–2181.
- DEEN, N. G., MUDDE, R. F., KUIPERS, J. A. M., ZEHNER, P. & KRAUME, M. 2000 Ullmanns encyclopedia of industrial chemistry, chapter bubble columns., Wiley-VCH Verlag GmbH & Co. KGaA.
- DEEN, N. G., VAN SINT ANNALAND, M. & KUIPERS, J. A. M. 2004 Multi-scale modelling of dispersed gas–liquid two-phase flow. *Chem. Engng Sci.* **59**, 1853–1861.
- DIJKHUIZEN, W., ROGHAI, I., VAN SINT ANNALAND, M. & KUIPERS, J. A. M. 2010 DNS of gas bubbles behaviour using an improved 3D front tracking model – drag force on isolated bubbles and comparison with experiments. *Chem. Engng Sci.* **65**, 1427–1437.

## *The clustering morphology of freely rising deformable bubbles*

- FERENC, J. S. & NÉDA, Z. 2007 On the size distribution of Poisson Voronoi cells. *Physica A: Stat. Mech. Appl.* **385**, 518–526.
- FIABANE, L., ZIMMERMANN, R., VOLK, R., PINTON, J.-F. & BOURGOIN, M. 2012 Clustering of finite-size particles in turbulence. *Phys. Rev. E* **86**, 035301.
- FRENKEL, D. & SMIT, B. 2002 *Understanding Molecular Simulation: From Algorithms to Applications*. Academic Press.
- MAGNAUDET, J. & MOUGIN, G. 2007 Wake instability of a fixed spheroidal bubble. *J. Fluid Mech.* **572**, 311–337.
- MARTÍNEZ MERCADO, J., CHEHATA-GÓMEZ, D., VAN GILS, D. P. M., SUN, C. & LOHSE, D. 2010 On bubble clustering and energy spectra in pseudo-turbulence. *J. Fluid Mech.* **650**, 287–306.
- MONCHAUX, R., BOURGOIN, M. & CARTELLIER, A. 2010 Preferential concentration of heavy particles: a Voronoi analysis. *Phys. Fluids* **22**, 103304.
- OKABE, A., BOOTS, B., SUGIHARA, K. & CHIU, S. N. 2000 *Spatial Tessellations*. Wiley.
- RIBOUX, G., RISSO, F. & LEGENDRE, D. 2010 Experimental characterization of the agitation generated by bubbles rising at high Reynolds number. *J. Fluid Mech.* **643**, 509–539.
- ROGHAIR, I., VAN SINT ANNALAND, M. & KUIPERS, J. A. M. 2012b Drag force and clustering in bubble swarms, *AIChE J.* (early view) doi:[10.1002/aic.13949](https://doi.org/10.1002/aic.13949).
- ROGHAIR, I., LAU, Y. M., DEEN, N. G., SLAGTER, H. M., BALTUSSEN, M. W., VAN SINT ANNALAND, M. & KUIPERS, J. A. M. 2011a On the drag force of bubbles in bubble swarms at intermediate and high Reynolds numbers. *Chem. Engng Sci.* **66**, 3204–3211.
- ROGHAIR, I., MARTÍNEZ MERCADO, J., VAN SINT ANNALAND, M., KUIPERS, J. A. M., SUN, C. & LOHSE, D. 2011 Energy spectra and bubble velocity distributions in pseudo-turbulence: numerical simulations vs. experiments. *Intl J. Multiphase Flow* **37**, 1093–1098.
- TAGAWA, Y., MERCADO, J. M., PRAKASH, V. N., CALZAVARINI, E., SUN, C. & LOHSE, D. 2012 Three-dimensional Lagrangian Voronoi analysis for clustering of particles and bubbles in turbulence. *J. Fluid Mech.* **693**, 201–215.
- TOSCHI, F. & BODENSCHATZ, E. 2009 Lagrangian properties of particles in turbulence. *Annu. Rev. Fluid Mech.* **41**, 375–404.
- UNVERDI, S. O. & TRYGGVASON, G. 1992 A front-tracking method for viscous, incompressible, multi-fluid flows. *J. Comput. Phys.* **100**, 25–37.
- YIN, X. & KOCH, D. L. 2008 Lattice-Boltzmann simulation of finite Reynolds number buoyancy-driven bubbly flows in periodic and wall-bounded domains. *Phys. Fluids* **20**, 103304.
- ZENIT, R., KOCH, D. L. & SANGANI, A. S. 2001 Measurements of the average properties of a suspension of bubbles rising in a vertical channel. *J. Fluid Mech.* **429**, 307–342.